Preferential turbulence enhancement in two-dimensional compressions

Seth Davidovits*
Lawrence Livermore National Laboratory, Livermore, California 94550, USA

Nathaniel J. Fisch
Department of Astrophysical Sciences, Princeton University, Princeton, New Jersey 08544, USA

(Received 21 August 2020; accepted 4 November 2020; published 23 November 2020)

When initially isotropic three-dimensional (3D) turbulence is compressed along two dimensions, the compression supplies energy directly to the flow components in the compressed directions, while the flow component in the noncompressed direction experiences the effects of compression only indirectly through the nonlinearity of the hydrodynamic equations. Here we study such 2D compressions using numerical simulations. For initially isotropic turbulence, we find that the nonlinearity can be insufficient to maintain isotropy, with the energy components parallel to the compression coming to dominate the turbulent energy, with a number of consequences. Among these are the possibilities for stronger and more easily sustained growth of turbulent energy than in 3D compressions and for an increasing turbulent Mach number even in a compression without thermal losses.

DOI: 10.1103/PhysRevE.102.053213

I. INTRODUCTION

The desire to understand the scaling of turbulent hydrodynamic energy under compression arises in a variety of settings, including combustion, aerodynamics, astrophysics [1–3], and inertial fusion [4–11]. Compression tends to inject energy into the turbulence, while turbulent dissipation (for example, through viscosity) removes turbulent energy. Together, the net balance of these effects (and possibly others) at each time determines whether the turbulence in the compression is growing or decreasing. The amount (as well as properties) of the turbulence then influences important dynamics in the various settings, ranging from material mixing (combustion and inertial fusion) to the density distribution (astrophysics and Z pinches [12]).

At present, we examine the turbulent kinetic energy (TKE) dynamics of a three-dimensional fluid (or plasma) undergoing compression in two dimensions. We do so by analyzing the result from numerical simulations. Specifically, we focus on the rate of change of the TKE in two-dimensional (2D) compressions with changing volume, which is tied to the degree to which the turbulence remains isotropic in the compression. Of particular note is that we find that a preferential enhancement of the TKE can occur in 2D compressions, which does not occur in 3D compressions. Throughout this work, when we refer to 3D compressions, we mean isotropic 3D compressions.

While we consider an idealized problem, in order to isolate basic effects, such effects may be of relevance to laboratory Z-pinch compression experiments, where a cylindrical plasma is compressed radially; such experiments underlie radiation or neutron sources [13], as well as a fusion experiment concept, magnetized liner inertial fusion (MagLIF) [14,15]. In the case of gas-puff Z pinches for radiation generation, observations suggest the presence of substantial turbulent energy at stagnation [12,16–18], which may be compressed during the course of the pinch. This phenomenon is likely relevant in higher-current gas-puff and wire-array Z pinches [19,20]. Laser preheat in MagLIF experiments may generate vorticity in the central fuel, which then undergoes substantial compression during the pinch [21].

Here it is useful to consider an analogy between the compression of TKE and the familiar case of the compression of thermal energy. In the simplest, lossless case (adiabatic for the thermal or turbulent energy), the thermal energy of an ideal monatomic gas grows as $V^{-2/3}$ as the volume V is compressed. This growth is independent of the manner of compression; that is, working in Cartesian coordinates, we may compress in one dimension (say, along x), two dimensions (say, along x and y), or three dimensions and the energy growth as a function of volume will be the same, assuming collisions happen rapidly enough to keep the thermal motions isotropic in the compression. The same would be true of the TKE, as it is considered here, if it remains isotropic during the compression. Further, the TKE would grow at the same $V^{-2/3}$ rate as the thermal energy [6,22,23]. In the case of the TKE, the nonlinearity of the Navier-Stokes (NS) equation plays the role of collisions, being the mechanism by which energy injected by the compression can equilibrate into the uncompressed flow component(s).

Here we investigate how effective the NS nonlinearity is at maintaining or restoring the isotropy of the TKE in compressions at various rates. If isotropy is *not* maintained, then the TKE may grow more rapidly as a function of volume than the $V^{-2/3}$ scaling. In this scenario the compression may inject more energy into the turbulent energy than the thermal energy per volume decrement, leading to preferential enhancement of the turbulence. While, in general real systems, both the

*davidovits1@llnl.gov

 ©2020 American Physical Society

thermal and turbulent energy dynamics are affected by a variety of other loss (or forcing) mechanisms, this basic question of TKE equilibration and the associated impact on TKE growth rate can remain relevant.

We find that in 2D compressions the TKE can become and remain highly anisotropic. As a consequence, the TKE in 2D compressions can grow more strongly than the ideal isotropic scaling of $V^{-2/3}$, with a scaling peaking at V^{-1}. This then distinguishes the TKE not only from the thermal energy in an ideal compression, but also from the TKE in a 3D compression, where isotropy is retained and a maximum growth of TKE as $V^{-2/3}$ can occur. Further, we discuss the likelihood that the TKE growth is more easily sustained in 2D compressions, due to aspect ratio effects.

The paper is organized as follows. In Sec. II we briefly cover the formulation of the 2D compression system which we use to investigate the problem at hand. The numerical simulations used for the study are described in Sec. II. Section III contains the main results, which are broken into two parts. First, Sec. III A describes the theoretical framework we analyze the results in, which examines the polytropic (or adiabatic) index for a turbulent pressure under compression. Second, Sec. III B contains simulation results and analysis, broken into three pieces: Sec. III B 1 shows simulation results and analysis for the 3D compression case to be contrasted with the 2D case; Sec. III B 2 shows the 2D compression case for the same initial conditions; Sec. III C shows the 2D compression case for an alternate initial condition, to gain further insight. Finally, we conclude in Sec. IV.

II. FORMULATION

To study the TKE behavior in two-dimensional compressions, we use an approach similar to substantial prior work on the compression of turbulence [5,22–25] and the same as that described in [11]. This approach is described again briefly here; more details, in the very similar 3D formulation, can be found in the Appendix of Ref. [5]. Because it will be a point of comparison, we also describe the 3D compression case simultaneously.

We take the gas or plasma behavior to be governed by the NS equations. A compression is caused by an assumed background flow field $v_{i0}(\mathbf{x},t) = A_{ij}(t)x_j$, with the complete NS flow given by $v_i(\mathbf{x},t) = v_{i0}(\mathbf{x},t) + v_i'(\mathbf{x},t)$. Our goal is to solve for the behavior of the (turbulent) field v_i' given the compressing background flow v_{i0}.

We will work in Cartesian coordinates throughout. A 3D isotropic compression occurs when $A_{ij}(t) = a(t)\delta_{ij}$ is diagonal (δ_{ij} is the Kronecker delta). A symmetric 2D compression occurs when $A_{ij}(t) = a(t)$ for $i = j = 1$ or $i = j = 2$ and $A_{ij}(t) = 0$ otherwise. In the present case, for two-dimensional compression, we take the compression directions to be x and y, with the z axis then uncompressed. Here we take

$$a(t) = \dot{L}/L, \tag{1}$$

with the overdot indicating a time derivative, and

$$L(t) = L_0 - 2U_b t. \tag{2}$$

The effect of the background flow is as follows. In a 3D compression, this background flow is such that a cube of initial side length L_0 placed in the background flow and advected by it will remain a cube, with a side length $L(t)$ that contracts at constant velocity according to Eq. (2). In a 2D compression, the (initial) cube will only contract along the x and y directions, with the side length along those axes given by $L(t)$, while the uncompressed z direction will have a constant side length of L_0.

We will assume that the perturbed flow v_i' is homogeneous under ensemble averaging and we will ignore density perturbations associated with it (low-Mach-number flow assumption). With no density perturbations, the complete density behavior is then simply given by $\rho_{2D}(t) = \rho_0/\bar{L}^2$ for the 2D case and $\rho_{3D}(t) = \rho_0/\bar{L}^3$ for the 3D case. Here $\bar{L}$ is the normalized contracting side length

$$\bar{L} = 1 - 2U_b t/L_0. \tag{3}$$

Explicit spatial dependence in the NS momentum equation can be eliminated by working in coordinates $\mathbf{X}$ that move with the background flow. In three dimensions, this is $\mathbf{x} = \bar{L}\mathbf{X}$, while in two dimensions it is $x = \bar{L}X$, $y = \bar{L}Y$, and $z = Z$. Writing $v_i'(\mathbf{x},t) = V_i(\mathbf{X},t)$ and $p'(\mathbf{x},t) = P(\mathbf{X},t)$, then for a 3D compression the NS momentum equations are

$$\frac{\partial V_i}{\partial t} + \frac{\dot{L}}{L}V_i + \frac{1}{\bar{L}}V_j\frac{\partial V_i}{\partial X_j} + \frac{\bar{L}^2}{\rho_0}\frac{\partial P}{\partial X_i} = \nu_0\bar{L}\bar{\mu}_{3D}\nabla^2 V_i, \tag{4}$$

while the continuity equation for the perturbed flow is simply the divergence-free constraint $\partial V_i/\partial X_i = 0$.

In the case of a 2D compression, the NS momentum equations are

$$\frac{\partial V_x}{\partial t} + \frac{\dot{L}}{L}V_x + \mathcal{C}(V_x) + \frac{\bar{L}}{\rho_0}\frac{\partial P}{\partial X} = \nu_0\bar{\mu}_{2D}\mathcal{D}(V_x), \tag{5}$$

$$\frac{\partial V_y}{\partial t} + \frac{\dot{L}}{L}V_y + \mathcal{C}(V_y) + \frac{\bar{L}}{\rho_0}\frac{\partial P}{\partial Y} = \nu_0\bar{\mu}_{2D}\mathcal{D}(V_y), \tag{6}$$

$$\frac{\partial V_z}{\partial t} + \mathcal{C}(V_z) + \frac{\bar{L}^2}{\rho_0}\frac{\partial P}{\partial Z} = \nu_0\bar{\mu}_{2D}\mathcal{D}(V_z), \tag{7}$$

while the continuity equation is

$$\frac{1}{\bar{L}}\left(\frac{\partial V_x}{\partial X} + \frac{\partial V_y}{\partial Y}\right) + \frac{\partial V_z}{\partial Z} = 0. \tag{8}$$

In Eqs. (5)–(7) we have used a shorthand operator form for both the convective term $\mathcal{C}$ and the viscous dissipation term $\mathcal{D}$,

$$\mathcal{C}(A) = \frac{1}{\bar{L}}\left(V_x\frac{\partial A}{\partial X} + V_y\frac{\partial A}{\partial Y}\right) + V_z\frac{\partial A}{\partial Z}, \tag{9}$$

$$\mathcal{D}(A) = \frac{\partial^2 A}{\partial X^2} + \frac{\partial^2 A}{\partial Y^2} + \bar{L}^2\frac{\partial^2 A}{\partial Z^2}. \tag{10}$$

In the moving coordinates, the equations for the perturbed (turbulent) flow V, in both the 2D and 3D cases, are similar to the usual NS equations, with the differences being time-dependent scalings appearing on some terms, as well as forcing associated with the compression. In the 3D case, the forcing, the second term on the left-hand side of Eq. (4), appears for all velocity components; each velocity component is forced the same in the isotropic compression.

In the 2D case [Eqs. (5)–(7)], the forcing only appears in the equations for the velocity components parallel to the

compressed directions (V_x and V_y). This means that V_z can only increase through the action of the nonlinear terms (convective and pressure) in Eq. (7). Since V_x and V_y are directly forced, we may expect an initially isotropic flow, with equal energy in each flow component, will only remain isotropic if the nonlinearity is effective at transferring energy to V_z.

Note that, because we are solving for a perturbed flow which we have assumed is of small Mach number, the pressure appearing in the momentum equations is essentially that of incompressible flow, which acts to keep the continuity equation satisfied despite the nonlinearity. The mean pressure in this case follows from the mean density behavior, $\rho_{2D}(t)$ or $\rho_{3D}(t)$, coupled with the ideal gas law and an assumption about the temperature behavior in the compression (say, adiabatic or isothermal, to give two possible examples).

The remaining piece to specify the compressing system(s) is the viscous behavior. The dynamic viscosity μ is written as $\mu_{2D} = \mu_0 \bar{\mu}_{2D}$ (similarly for three dimensions) and the kinematic viscosity appearing in the 2D and 3D momentum equations is $\nu_0 = \mu_0/\rho_0$. If we utilize the unmagnetized Braginskii viscosity [26], then $\mu \sim \mu(\bar{T}, \bar{Z})$, with $\bar{T} = T/T_0$ the temperature normalized to its initial value and $\bar{Z} = Z/Z_0$ the ionization state normalized to its initial (spatially uniform) value. The impact of a changing plasma viscosity on the evolution of the TKE has been previously investigated in three-dimensional [4–9] and two-dimensional compressions [11].

For simplicity, consider the case of a fully ionized plasma (constant Z). Then, for the Braginskii viscosity, $\mu \propto \bar{T}^{5/2}$, where in the present work the temperature is treated as spatially uniform. For an adiabatic compression, we have $\bar{T}_{3D} = \bar{L}^{-2}$ and $\bar{T}_{2D} = \bar{L}^{-4/3}$. However, the temperature behavior growth in a real compression can be reduced by loss mechanisms, such as conduction or radiation, leading to weaker viscosity changes. We can consider a general (but still power-law) temperature behavior with compression by introducing a parameter β such that $\bar{\mu}_{3D} = \bar{L}^{-2\beta}$, while for 2D compressions we define $\bar{\mu}_{2D} = \bar{L}^{-4\beta/3}$; in either case β is a parameter determined by the net heating and cooling (and also possibly ionization) processes in the compression [5,27]. These definitions make it so that for a given β, the 2D and 3D compressions have the same dynamic viscosity as a function of volume, $\bar{\mu}_{2D}(V) = \bar{\mu}_{3D}(V)$.

Our primary goal here is to examine, with the aid of direct numerical simulation (DNS), the question of isotropization through the nonlinearity and the associated maximum sustained TKE growth, rather than effects due to changing viscosity (the viscosity can become quite large in certain plasma compressions, causing a transition from high to low Reynolds number [28]). In a truly high-Reynolds-number regime, changes in the viscosity can be verified to not influence the results of DNS of turbulence [29]. Thus, we would like our simulations to start and stay with a high Reynolds number, however, we also want the simulations to remain resolved at the smallest (viscous) scales as the compression progresses.

Since the energy injection from the compression can lead to increasing turbulent velocities, it can also then lead to increasing Reynolds numbers (and therefore resolution requirements for DNS). The Reynolds number will also be influenced by the viscous behavior. At present, to try to maintain both a reasonable Reynolds number and numerical resolution, as well as for physical convenience, we will study the case when $\beta = 3/2$, corresponding to $\bar{\mu}_{2D} = \bar{L}^{-2}$. For a fully ionized plasma (constant Z) with a Braginskii viscosity this corresponds to $\bar{T} = \bar{L}^{-4/5}$, since the temperature dependence of the Braginskii viscosity is proportional to $T^{5/2}$.

It is convenient, both for analysis and for numerical simulation, to rescale the fields and the time variable in the compressing frame momentum Eqs. (4) or (5)–(7), with a time-dependent scaling [5,6,30]. For the 3D case, we use the velocity scaling $V_i = \bar{L}^{\delta}\hat{V}_i$; for the 2D case, we use $V_{x,y} = \bar{L}^{\delta}\hat{V}_{x,y}$ for the x and y directions and $V_z = \bar{L}^{\sigma}\hat{V}_z$ for the z direction. We also scale the pressure $P = \bar{L}^{\eta}\hat{P}$ and the time $d\hat{t} = \bar{L}^{\tau}dt$.

Selecting, for the 3D case, $\delta = -1$, $\tau = -2$, and $\eta = -5$, we find, for the momentum Eq. (4),

$$\frac{\partial \hat{V}_i}{\partial \hat{t}} + \hat{V}_j \frac{\partial \hat{V}_i}{\partial X_j} + \frac{1}{\rho_0}\frac{\partial \hat{P}}{\partial X_i} = \nu_0 \bar{L}^{3-2\beta}\nabla^2 \hat{V}_i. \tag{11}$$

Examining Eq. (11), we see that in the special case of $\beta = 3/2$, the evolution of the turbulence under compression is determined by the solution of the NS equations for decaying turbulence [6,30].

In the 2D case, if we again select $\delta = -1$ and $\tau = -2$ and also select $\eta = -4$ and $\sigma = -2$, then the continuity Eq. (8) becomes simply the divergence-free constraint $\partial \hat{V}_i/\partial X_i = 0$. The momentum Eq. (5)–(7) become

$$\frac{\partial \hat{V}_x}{\partial \hat{t}} + \hat{V}_j \frac{\partial \hat{V}_x}{\partial X_j} + \frac{1}{\rho_0}\frac{\partial \hat{P}}{\partial X} = \nu_0 \bar{L}^{2-4\beta/3}\mathcal{D}(\hat{V}_x), \tag{12}$$

$$\frac{\partial \hat{V}_y}{\partial \hat{t}} + \hat{V}_j \frac{\partial \hat{V}_y}{\partial X_j} + \frac{1}{\rho_0}\frac{\partial \hat{P}}{\partial Y} = \nu_0 \bar{L}^{2-4\beta/3}\mathcal{D}(\hat{V}_y), \tag{13}$$

$$\frac{\partial \hat{V}_z}{\partial \hat{t}} - 2\bar{L}\dot{\bar{L}}\hat{V}_z + \hat{V}_j \frac{\partial \hat{V}_z}{\partial X_j} + \frac{\bar{L}^2}{\rho_0}\frac{\partial \hat{P}}{\partial Z} = \nu_0 \bar{L}^{2-4\beta/3}\mathcal{D}(\hat{V}_z). \tag{14}$$

Simulations

We now briefly describe the simulations used in the present work, which are similar to those in Refs. [11,27]. We utilize the pseudospectral code DEDALUS [31] to solve for the evolution of initially isotropic, homogeneous, turbulence under two-dimensional compression, as governed by Eqs. (5)–(8). We use periodic boundary conditions and a Fourier basis.

In DEDALUS it is numerically advantageous to solve rescaled equations and then unscale the results appropriately. For $\beta = 3/2$, we numerically solve Eqs. (12)–(14) together with the divergence-free constraint on $\hat{V}$.

We generate the initial state that is compressed in two different ways, which yield different initial spectral energy distributions. First we describe the method used for the results shown in Secs. III B 1 and III B 2, as well as the simulations in those sections. Following that, we describe the method used for the results shown in Sec. III C. All simulations have $\rho_0 = 1$, $L_0 = 1$, and $\nu_0 = 1/600$.

To generate the first initial state that is compressed, we initialize a divergence-free flow field with (uniformly distributed) random Fourier phases and magnitudes set proportional to $k^2 \exp[-(k_p/k)^2]$, with $k_p = 4$. This state is then

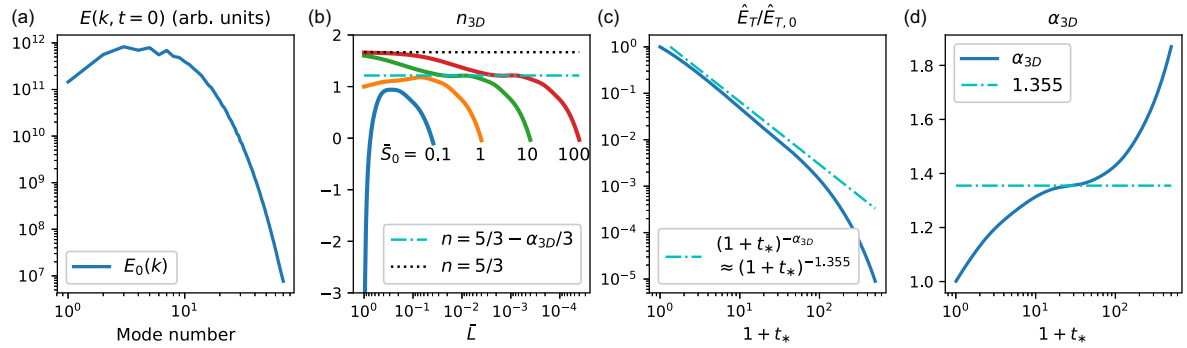

FIG. 1. Three-dimensional compression of an initial turbulent flow field (see Sec. III B 1); (a) isotropic power spectrum of the initial state before compression begins, (b) polytropic index n_{3D} [Eq. (18)] versus linear compression ratio $\bar{L}$ (time progresses left to right) for compression at different initial values of the compression rate $\bar{S}$ [Eq. (20)], (c) decay of energy associated with the scaled NS momentum equation (11) versus a scaled time which is related to $\bar{L}$ by Eq. (29) (compression progresses left to right), and (d) instantaneous inferred decay power, assuming a power-law decay for the scaled energy (30), which is seen to increase in time (as the compression progresses), eventually leading to the decrease in n_{3D} observed in (b).

allowed to decay (by the NS equations) for approximately a turnover time. The resulting flow field has an isotropic energy spectrum shown in Fig. 1(a).

The simulation to generate the initial state through decay uses a Fourier mode resolution of 216^3, which is 144^3 after 3/2 dealiasing. The results on 3D compression, shown in Figs. 1(b)–1(d), are computed with this same resolution. For the 2D compression results up to $\bar{L} = 0.03$ we use a grid of $216^2 \times 1236$ (dealiased to $144^2 \times 864$). The higher mode resolution is in the z direction, which is done because the form of the dissipation (10) allows for much steeper gradients (in the moving coordinates) along z at a given ν_0 as $\bar{L}$ shrinks in the compression. To continue 2D compressions past $\bar{L} = 0.03$ we add additional k_z modes at this $\bar{L}$ (time) to maintain resolution in this direction, resulting in a resolution before de-aliasing of $216^2 \times 2592$; this is done for the $\bar{S}_0 \approx 1$ and $\bar{S}_0 \approx 10$ cases shown in Fig. 2 and the following figures.

The initial field we use has the following properties, with angular brackets denoting a spatial average.

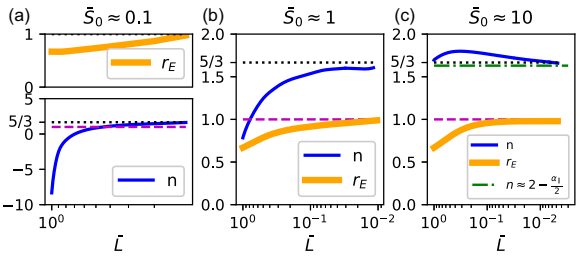

FIG. 2. Two-dimensional compression of the same initial state used for the 3D compression cases in Fig. 1, at comparable initial compression rates (see Sec. III B 2). Shown are the polytropic index n_{2D} [Eqs. (23) and (25)] versus compression ratio $\bar{L}$ (time progresses left to right in each plot). Also shown is the energy ratio r_E [Eq. (24)], which is a measure of the anisotropy of the turbulent flow. Three compression rates are shown, ranging from (a) an initially slow compression $\bar{S}_0 \approx 0.1$ to (b) $\bar{S}_0 \approx 1$ to (c) an initially fast compression $\bar{S}_0 \approx 10$.

The turbulent energy $E_{K,0} = \langle V_i V_i/2 \rangle \approx 0.85$, the dissipation $\epsilon_0 = -\nu_0 \langle V_i \nabla^2 V_i \rangle \approx 11.5$, and a derived Taylor microscale Reynolds number $\mathrm{Re}_\lambda = 2E_K\sqrt{5/3\epsilon_0\nu_0} \approx 16$. The initial decay time $\tau_{d,0} = (E_K/\epsilon)_0 \approx 0.074$.

We have also simulated 2D compressions of initial states generated using an alternate technique, the forcing method described by Lundgren [32] and Rosales and Meneveau [33], and these results are shown in Sec. III C. This forcing technique results in rather flat low-mode energy spectra [see Fig. 9(d)]. We generate the initial state in this case again using a resolution of 216^3 (dealiased to 144^3), which is then interpolated to the finer grid before the compression is started; the finer resolution ($324^2 \times 1236$) in x and y was used for the compressing simulations as part of checking convergence. In the case of the most dramatic compression shown $\bar{S}_0 \approx 20$, we restart part way through with a resolution of $324^2 \times 3888$, to maintain resolution in the z direction, as before.

The initial field that results from this second forcing scheme has the following properties, with angular brackets denoting a spatial average. The turbulent energy $E_K = \langle V_i V_i/2 \rangle \approx 0.97$, the dissipation $\epsilon = -\nu_0 \langle V_i \nabla^2 V_i \rangle \approx 2.57$, and a derived Taylor microscale Reynolds number $\mathrm{Re}_\lambda \approx 38$.

III. ANALYSIS AND RESULTS

The primary analysis and results are contained in Secs. III A and III B below. First, in Sec. III A we derive the polytropic index relation for 2D compression of hydrodynamic turbulence and compare it with the result for 3D compression. This provides our general framework for considering the TKE behavior during compression. Second, Sec. III B provides further analysis of these relations and a comparison to simulation results.

A. Turbulent polytropic (adiabatic) index

We find it useful to frame the TKE dynamics of a compressing flow in terms of a polytropic index (sometimes also referred to as the adiabatic index and denoted by γ). Here,

where the viscosity enters, we write it generally, without specializing to the power-law form discussed above. We start by recalling the familiar case of thermal pressure and energy evolution, which will be a useful point of comparison. When a plasma or monatomic gas that is treated as ideal undergoes an adiabatic compression, the thermal pressure p obeys a polytropic law

$$pV^n = C \tag{15}$$

and the polytropic index $n = 5/3$. Here V is the volume and C is a constant. Correspondingly, the thermal energy $U = 3pV/2$ grows as $V^{-2/3}$ in the compression. Assuming we are in a regime where collisions are able to rapidly (compared to the compression rate) isotropize thermal motions, these thermal pressure and energy scalings will hold independently of whether the compression is one, two, or three dimensional. That is, working in Cartesian coordinates, we will have $n_{\rm thermal} = 5/3$ whether we compress along only x, along x and y, or along x, y, and z.

An analogous polytropic index can be defined for the turbulence in both 3D [10] and 2D compressions. In the case of 3D compression, we write the equation for the time rate of change of the total TKE dE_T/dt, where $E_T = \iiint_{-L_0/2}^{L_0/2} d\mathbf{X}(\rho_0 V_i V_i/2)$. This total energy is the same as in the laboratory frame (in the laboratory frame, the density increases, but the volume to be integrated decreases in a manner that balances it). We use Eq. (4) to write the equation for dE_T/dt, use the volume relation $dV = 3L^2\dot{L}dt$ to rewrite it in terms of the volume rate of change, and define the viscous dissipation $\epsilon_\mu = -\mu\bar{L}\iiint_{-L_0/2}^{L_0/2} d\mathbf{X} V_i \nabla^2 V_i$. Doing so, we arrive at

$$-\frac{dE_T}{dV} = \frac{2}{3}\frac{E_T}{V} - \tau_c\frac{\epsilon_\mu}{3V}, \tag{16}$$

where we have defined the (positive) compression timescale as

$$\tau_c = -L/\dot{L}. \tag{17}$$

It is natural to define the turbulent pressure in this 3D compression as $p_{3D} = 2E_T/3V$, since, in Eq. (16), it is the quantity that relates the infinitesimal volume increment to the energy injected into the (turbulent) flow. The polytropic relation (15) implies $n = \partial \ln p/\partial \ln \rho$. With p_{3D} as just defined and Eq. (16), we find

$$n_{3D} = \frac{5}{3} - \frac{2}{3}\frac{\tau_c}{\tau_t} = \frac{5}{3} - \frac{2}{3}\frac{1}{\bar{S}}, \tag{18}$$

where the turbulent turnover time in this case is defined as

$$\tau_t = \frac{2E_T}{\epsilon_\mu} = 2\tau_d, \tag{19}$$

with τ_d the decay timescale $\tau_d = -E_T/\dot{E}_T = E_T/\epsilon_\mu$. We have defined a normalized strain rate $\bar{S}$ as

$$\bar{S} = \frac{\tau_t}{\tau_c}. \tag{20}$$

With these definitions, an isoturbulent contraction ($n = 1$) occurs if $\tau_c = \tau_t$ or $\bar{S} = 1$ (see Ref. [5] for examples of 3D contractions that reach this state, or for an example in the inertial confinement fusion context, Ref. [27]). The ratio τ_c/τ_t and $\bar{S}$ can also be written as a type of Reynolds number. A compression is rapid if $\tau_c \ll \tau_t$ and $\bar{S} \gg 1$, which leads to amplification of the TKE with $n_{3D} \to 5/3$, the peak achievable amplification rate in this treatment. If the compression is very slow $\tau_t \ll \tau_c$, $\bar{S} \ll 1$, and n_{3D} can take negative values. In this case, the turbulence dissipates before it experiences the compression.

For 2D compressions, we follow a similar procedure, accounting for the volume in this case being $V = L_0L^2$. The equation for the total energy in a 2D compression is

$$-\frac{dE_T}{dV} = \frac{E_\parallel}{V} - \tau_c\frac{\epsilon_{\mu,2D}}{2L_0^3\bar{L}^2}. \tag{21}$$

Here the 2D viscous dissipation is $\epsilon_{\mu,2D} = -\mu\iiint_{-L_0/2}^{L_0/2} d\mathbf{X} V_i \mathcal{D}(V_i)$ and the parallel (to compression) energy $E_\parallel = \iiint_{-L_0/2}^{L_0/2} d\mathbf{X}\rho_0(V_x^2 + V_y^2)/2$.

In this case, only flow in the directions parallel to the compression (V_x and V_y) is associated with a turbulent pressure; that is, the energy injected by an infinitesimal contraction only depends on these components. Then the natural definition of turbulent pressure is $p_{2D} = E_\parallel/V$. As such, in order to find $n_{2D} = \partial \ln p_{2D}/\partial \ln \rho_{2D}$, we use Eqs. (5) and (6) to write an equation for the time (volume) evolution of $E_\parallel$ and find, for n_{2D},

$$n_{2D} = 2 + \tau_c\frac{T_\parallel}{E_\parallel} - \tau_c\frac{\epsilon_{\mu,\parallel}}{E_\parallel}. \tag{22}$$

The parallel viscous dissipation $\epsilon_{\mu,\parallel} = \mu\iiint_{-L_0/2}^{L_0/2} d\mathbf{X}$ $[V_x\mathcal{D}(V_x) + V_y\mathcal{D}(V_y)]$, while $T_\parallel = \iiint_{-L_0/2}^{L_0/2} d\mathbf{X}\{V_x[\rho_0 C(V_x)$ $+ \bar{L}\partial_X P] + V_y[\rho_0 C(V_y) + \bar{L}\partial_Y P]\}$ represents the nonlinear transfer of energy between $E_\parallel$ and the uncompressed direction energy $E_\perp = E_z = \iiint d\mathbf{X}\rho_0 V_z^2/2$. There is no corresponding nonlinear transfer term appearing in n_{3D} [Eq. (18)] because the transfer is conservative and integrates out when the full energy evolution is considered.

As before, we can define additional timescales to write n in terms of timescale ratios. In this case we define a nonlinear transfer timescale $\tau_{\rm nl} = -2E_\parallel/3T_\parallel$ and the turbulent turnover time $\tau_{t,\parallel} = 4E_\parallel/3\epsilon_{\mu,\parallel}$. Then

$$n_{2D} = 2 - \frac{1}{3}\frac{\tau_c}{\tau_{\rm nl}} - \frac{2}{3}\frac{\tau_c}{\tau_{t,\parallel}}. \tag{23}$$

The numerical coefficients in the definitions of the timescales $\tau_{\rm nl}$ and $\tau_{t,\parallel}$ are chosen so that for $\tau_c = \tau_{\rm nl}$ and $\tau_c = \tau_{t,\parallel}$ we have $n = 1$, and the coefficient in the definition of $\tau_{\rm nl}$ is selected so that $n = 5/3 - \tau_c\epsilon_{\mu,\parallel}/E_\parallel$ when $\tau_{\rm nl} = \tau_c$.

By defining the energy ratio

$$r_E = \frac{E_\parallel}{E_T} = \frac{E_\parallel}{E_\parallel + E_z}, \tag{24}$$

it is possible to recast n_{2D} in an alternate but equivalent form

$$n_{2D} = 1 + r_E - \frac{\partial \ln r_E}{\partial \ln V} - \frac{2}{3}\frac{\tau_c}{\tau_{t,T}}. \tag{25}$$

In this case the turbulent turnover time $\tau_{t,T} = 4E_T/3\epsilon_{\mu,2D}$. In (statistically) isotropic turbulence, the energy ratio $r_E \sim 2/3$. We will find both forms of n_{2D} [Eqs. (23) and (25)] useful in the analysis of 2D compressions.

B. TKE growth and anisotropy

1. Behavior of n_{3D}

Before addressing the values and behavior of n_{2D}, we discuss n_{3D} [Eq. (18)]. When, as is presently the case, the compression rate is predetermined, τ_c is a known function of time [Eq. (17)]. Then n_{3D} is determined by the evolution of the turbulent turnover timescale τ_t [Eq. (19)]. In general, determining the evolution of τ_t is a difficult problem, requiring the solution of the (turbulent) Navier-Stokes equation, including possibly time-varying viscosity (4) or equivalently (11).

Existing turbulence models for 3D compression with viscosity variation determined by the $\beta = 5/2$ case [7] or for the general β case [6] can then be used to model n_{3D}. When the viscosity stays steady or increases in the compression, the general trend for an initially fast compression is as follows. In an initially fast compression, $\tau_{c,0} \ll \tau_{t,0}$ ($\bar{S}_0 \gg 1$), so $n_{3D,0} \sim 5/3$. However, the turbulence will tend to evolve towards faster timescales at a rate such that the ratio $\bar{S}$ decreases, and thus n_{3D} will decrease in time from the initial value $\sim 5/3$. When the viscosity growth with compression is $\beta > 1$, the turbulence will eventually dissipate with continued compression [5] so that n becomes less than one (in practice n can become negative). When $\beta = 1$, it can be shown that the turbulence saturates with continued compression so that $n_{3D} \to 1$ (assuming an initial compression rate that meets a threshold condition) [5].

Figure 1(b) shows $n_{3D}(\bar{L})$ for compression with a range of initial rates $\bar{S}_0$ for the case when $\beta = 3/2$. The trends just described are visible. Additionally, for $\bar{S}_0 = 10$ and 100, we observe a regime with n_{3D} approximately constant. We now explain this plateau regime.

Consider n_{3D} in an initially fast compression when $\beta = 3/2$. Initially, $n_{3D} \sim 5/3$ due to the fast compression, and ultimately n_{3D} in this case will become less than one as the TKE dissipates (due to the rate at which the viscosity increases with the increasing temperature in the compression, relative to the rate of TKE injection). Both of these behaviors can be governed by linear effects. When the compression is rapid and $n \sim 5/3$, this is a result of the TKE evolution being controlled by the linear forcing from the compression, the second term on the left-hand side of Eq. (4). When the viscosity grows very large and n_{3D} becomes highly negative as the TKE dissipates, the behavior can be controlled by the linear viscous term, the right-hand side of Eq. (4). If the initial Reynolds number is high enough, there exists an intermediate regime where nonlinear evolution of the turbulence governs n_{3D}.

In the $\beta = 3/2$ case, we now determine the value of n_{3D} in this intermediate, nonlinear, stage. For $\beta = 3/2$, the scaled NS equation for the compression (11) is just the "usual" incompressible NS equation. In this case, at high Reynolds number, the energy evolution can be modeled as a power-law decay

$$\hat{E}_T(\hat{t}) = \iiint_{-L_0/2}^{L_0/2} d\mathbf{X} \rho_0 \hat{V}_i \hat{V}_i / 2 = \hat{E}_{T,0}(1 + \hat{t}/t_0)^{-\alpha_{3D}}, \quad (26)$$

with a decay power α_{3D} and a decay timescale t_0. The laboratory frame energy is simply related to the scaled energy $E_T = \bar{L}^{-2}\hat{E}_T$. In general, α_{3D} depends on the slope of the TKE power spectrum at low wave numbers (long wavelength) (see, e.g., Ref. [34]). Note that, for a given observed decay, the value of t_0 can also affect the inferred value of α_{3D} (see, e.g., Ref. [35] for more discussion); here, motivated by other work [36], we use $t_0 = \tau_{d,0} = \tau_{t,0}/2$ consistently throughout, including later for 2D compressions (which start from an identical initial state).

Figure 1(c) shows the decay of the total TKE for the present initial condition, plotted against a normalized time t_*,

$$t_* = \frac{\hat{t}}{\tau_{d,0}} = \frac{2\hat{t}}{\tau_{t,0}}. \quad (27)$$

By undoing the velocity and time scalings (converting back to the variables without a circumflex), we can write the time (or, more conveniently, $\bar{L}$) evolution of the laboratory frame TKE $\bar{E}_T(\bar{T}) = E_T/E_{T,0} = [1 + (-1 + 1/\bar{L})(2/\bar{S}_0)]^{-\alpha_{3D}}/\bar{L}^2$ and from that calculate $n_{3D} = 1 - (\bar{L}/3\bar{E}_T)d\bar{E}_T/d\bar{L}$ in the high-Reynolds-number limit

$$n_{3D} \to \frac{5}{3} - \frac{\alpha_{3D}}{3}\frac{1}{1 + \bar{L}(\bar{S}_0/2 - 1)} \sim \frac{5 - \alpha_{3D}}{3}. \quad (28)$$

Since we have scaled time as $d\hat{t} = \bar{L}^{-2}dt$ (for both 3D and 2D cases), the relation between t_* and $\bar{L}$ is given by

$$\bar{L} = \frac{1}{1 + \bar{S}_0 t_*/2}. \quad (29)$$

Figure 1(c) shows a fit (dash-dotted) line $\hat{E}_T \sim (1 + t_*)^{-1.355}$, which can be seen to match (approximately) the slope of the decay over a period around $t_* \sim 10$ (discussed below). This then corresponds to $\alpha_{3D} \approx 1.355$. Figure 1(b) shows (dash-dotted line) Eq. (28) with this value of α_{3D}; it agrees with the value of n_{3D} in the observed plateau regime.

In general, the value of α_{3D} can change during the compression. Figure 1(d) shows the instantaneous inferred value of α_{3D} as a function of t_* during the decay. This is calculated from the assumed power-law decay (26) as

$$\alpha_{3D}(t_*) = \frac{\ln(\hat{E}_T/\hat{E}_{T,0})}{\ln[1/(1 + t_*)]}. \quad (30)$$

It can be seen that α_{3D} increases in time during the decay for this initial condition, with a plateau around $\alpha_{3D} \approx 1.355$, yielding $n_{3D} \approx 1.22$. An important note is that the relation (28) is written for *constant* α_{3D}; when α_{3D} changes in time, there should be another term entering the equation, which depends on this rate of change with $\bar{L}$ (time). This extra term, ignored here, is the reason the dash-dotted line in Fig. 1(c) only approximately matches the apparent slope of $\ln(\hat{E}_T)$ vs $1 + t_*$ in Fig. 1(c) [the true fit at this time is closer to $(1 + t_*)^{-1.4}$]. Later, in Sec. III C, for the 2D compression case, we treat the impact of time-varying α.

As previously stated, the value of α_{3D} depends on the slope of the power spectrum at small (Fourier) wave number k, $E_T(k) \sim k^s$. For example, the Kolmogorov (or Batchelor) decay result is $\alpha_{3D} = 10/7$ ($s = 4$), while the Saffman result is $\alpha_{3D} = 6/5$ ($s = 2$) [37]. These then correspond to $n_{3D} = 25/21 \approx 1.19$ and $n_{3D} = 19/15 \approx 1.27$, respectively, in the nonlinear cascade regime. Rewritten in terms of the energy growth rate, these results agree with those given for the cascade regime in [7]. While we began by considering a specific

viscosity dependence $\beta = 3/2$, this dependence does not actually enter into the present result for n_{3D} in the nonlinear phase.

The high-Reynolds-number limit of the decay, which is utilized to arrive at Eqs. (26) and (28), can only hold for so long when $\beta > 1$; eventually, the viscous regime is reached and the decay characteristics will change, with α increasing, leading to a decrease in n [6,7]. This is observable in Fig. 1. When $\beta = 1$, the turbulence can saturate in length scale at the (simulation or physical) domain size, yielding a change in α ($\alpha \to 2$ [38,39]). A more broadly applicable version of Eq. (28), capturing these variations, is possible, e.g., through the use of more complex decay treatments than Eq. (26) [6,7,40].

2. *Two-dimensional compressions and n_{2D}*

Examining Eqs. (23) and (25), we can immediately make some observations. First, from Eq. (23), we can see that $n_{2D} > 5/3 = n_{3D,\max}$ may be achieved, depending on the values taken by the timescales entering the equation. Note that τ_c and $\tau_{t,\parallel}$ are generally non-negative, while in principle τ_{nl} can be either positive or negative, corresponding to energy transfer out of or into $E_\parallel$, respectively. However, we consider initially isotropic states, and in the 2D compressions only $E_\parallel$ is forced; as such, we may expect that the tendency at present is for the nonlinearity to transfer energy from $E_\parallel$ to E_z, corresponding to $\tau_{nl} \geqslant 0$. This is what we observe in simulations (except for very small initial compression rates $\bar{S}_0 \sim 0.01$, where the sign is observed to switch back and forth, not shown here). Then $n_{2D} \leqslant 2$, with both the nonlinearity and the turbulent dissipation tending to decrease the rate of (parallel) energy growth in the compression.

A second observation, from Eq. (25), is that if $r_E = 2/3$ (the isotropic value) and stays this value in the compression, then $n_{2D} = 5/3 - 2\tau_c/3\tau_{t,T}$. That is, if isotropy of the energy is maintained in the compression, the turbulent growth is capped at the same rate as for 3D compression, $n_{2D} \leqslant 5/3$, as one expects.

For $\beta = 3/2$, Fig. 2 shows the $\bar{L}$ (time) evolution of n_{2D} and r_E for 2D compressions of the same initially isotropic state at three different rates $\bar{S}_0$,

$$\bar{S}_0 = \frac{3}{2}\left(\frac{\tau_{t,T}}{\tau_c}\right)_0, \tag{31}$$

with values $\bar{S}_0 \approx 0.1, 1, 10$. Note that $\bar{S}_0$ in Eq. (31) is defined such that it is identical, at $t = 0$ and $\bar{L} = 1$, to $\bar{S}$ as written in Eq. (20). In other words, the initial compression rate is normalized to the same initial turnover time for both 2D and 3D compressions.

A few things are immediately of note in Fig. 2. First, the fraction of the energy in the parallel components r_E [Eq. (24)] generally increases from the equilibrium value of 2/3 as the compression progresses in all cases, moving towards the maximum value of $r_E \sim 1$. This indicates that the energy becomes highly anisotropic as the compression progresses. Second, the fast compression $\bar{S}_0$ achieves $n_{2D} > 5/3$ for a substantial duration of compression; thus this rate exceeds the maximum growth rate for 3D compressions and also the adiabatic growth rate of thermal energy. Third, in no cases do we see a drastic falloff of n_{2D} under compression (up to the minimal simulated

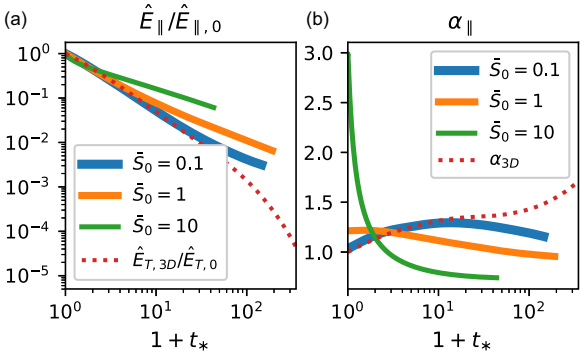

FIG. 3. For the 2D compressions shown in Fig. 2, the decay of the scaled parallel energy, associated with the scaled NS equations for 2D compression (12) and (13) (see Sec. III B 2: (a) the (scaled) energy behavior versus time (increasing compression left to right) and (b) the instantaneous inferred decay power assuming a power-law decay as in Eq. (30), but for $E_\parallel$ and $\alpha_\parallel$. Shown for comparison is the 3D compression behavior of scaled energy and decay power, for the identical initial condition (in the 3D case, the plotted results hold for *all* initial compression rates). The smaller, and decreasing, decay rates in 2D compression lead to a higher, and more sustained, polytropic index for the turbulence.

$\bar{L}$), as we do in the 3D compressions shown in Fig. 1. We now discuss these points in more detail.

As in the analysis of the 3D compression case, we find it useful to examine the scaled equations, in this case Eqs. (12) and (13), which govern the evolution of the (scaled) parallel energy $\hat{E}_\parallel$. Recall that this energy is simply related to the laboratory frame parallel energy as $E_\parallel = \bar{L}^{-2}\hat{E}_\parallel$. As in the 3D case, these equations no longer have forcing due to the compression; then, to the extent that the nonlinearity tends to transfer energy out of $\hat{E}_\parallel$, which we find to be the case at these compression rates (Fig. 4, discussed later), these are equations

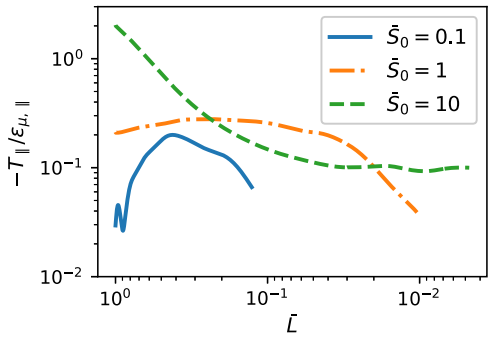

FIG. 4. Relative contributions to n_{2D} of transfer to E_z ($T_\parallel$) versus viscous dissipation of $E_\parallel$ for the 2D compression cases shown in Fig. 2 [see Eq. (35) and Sec. III B 2]. When $-T_\parallel/\epsilon_{\mu,\parallel}$ (y value) is less than 1, n_{2D} is determined primarily by viscous dissipation of $E_\parallel$; in the opposite limit, it is determined primarily by transfer of energy from the compressed directions $E_\parallel$ to the uncompressed direction energy E_z.

for the decay of $\hat{E}_\parallel$ at constant viscosity (since $\beta = 3/2$ at present).

Writing this decay in the form of an (assumed) power law, as in the 3D case,

$$\hat{E}_\parallel = \hat{E}_{\parallel,0}(1+\hat{t}/t_0)^{-\alpha_\parallel}. \tag{32}$$

The instantaneous decay rate $\alpha_\parallel$ can be solved for, giving Eq. (30), but with $\hat{E}_T \to \hat{E}_\parallel$ and $\alpha_{3D} \to \alpha_\parallel$.

Using the decay equation for $\hat{E}_\parallel$, we can write n_{2D} in terms of the decay rate, as we did for the 3D case in Eq. (28),

$$n_{2D} \to 2 - \frac{\alpha_\parallel}{2}\frac{1}{1+\bar{L}(\bar{S}_0/2-1)}(1+\chi) \sim 2 - \frac{\alpha_\parallel}{2}, \tag{33}$$

$$\chi = \frac{\partial \ln \alpha_\parallel}{\partial t_*}\ln[(1+t_*)^{(1+t_*)}]. \tag{34}$$

While in the 3D case we assumed α was constant, here we write the expression accounting for the time ($\bar{L}$) varying decay rate. If the decay rate is constant, $\chi = 0$. We write χ using t_* for conciseness; $\chi(\bar{L})$ is found utilizing Eq. (29).

From Eqs. (33) and (34) we see that if $\alpha_\parallel$ decreases with compression (increasing t_* and decreasing $\bar{L}$), this causes an increase in n_{2D} relative to the prediction assuming constant $\alpha_\parallel$ at the instantaneous value. Comparing Eq. (33) to the 3D case [Eq. (28)], we can see that if it were the case that $\alpha_\parallel \sim \alpha_{3D}$, n_{2D} and n_{3D} in the nonlinear phase would not be so different. That is, if the decay rate of the (scaled) parallel energy in two dimensions were similar to the decay rate for the (scaled) 3D energy, the differences in turbulence enhancement in 2D or 3D compression would be slight. Consider, for example, $\alpha = 1.355$ as observed for our 3D simulation, which yields, for the nonlinear regime, $n_{3D} \approx 1.22$ and $n_{2D} = 1.32$. This difference would be decreased for higher decay rates (disappearing at $\alpha = 2$).

Figure 3(a) shows the time evolution of $\hat{E}_\parallel$ for each value of $\bar{S}_0$ from Fig. 2, and in Fig. 3(b) the corresponding instantaneous decay rate $\alpha_\parallel(t_*)$ inferred from this decay is shown. Also shown are the results from the 3D decay, from Fig. 2. Since, in all cases, the evolution is governed by similar decaying NS equations starting from the same initial state, all cases are comparable as a function of t_*. The cases differ as a function of $t_* \propto \hat{t}$ for two reasons. First, $\bar{L}$, which can be thought of as a function of $\bar{S}_0$ and $\hat{t}$ [Eq. (29)], enters into the viscous dissipation term D [Eq. (10)]. Second, $\bar{L}$ appears explicitly in the evolution of $\hat{V}_z$ [Eq. (14)], which in turn appears in the nonlinear term in the $\hat{V}_x$ and $\hat{V}_y$ equations.

There are two key features to note in Fig. 3. First, the energy decay as a function of t_* occurs more slowly with increasing $\bar{S}_0$, observed in Fig. 3(a) and appearing in Fig. 3(b) as a lower inferred $\alpha_\parallel$ at later times. Second, $\alpha_\parallel$ tends to *decrease* (monotonically for $\bar{S}_0 = 1, 10$), while for the 3D case for the same initial condition the decay rate increases as the decay progresses. Taken together, these suggest that the growth rate of TKE in 2D compressions can be both larger and more sustainable than in 3D compressions, within the scope of the treatment here.

One possible concern in interpreting these observations is that one could make similar observations from the *linear* solution to the 2D compression system. When $\beta = 3/2$, the linear solution (including viscosity) to the 2D compression system can give $n_{2D} \to 2$ for large compression, consistent with the scaled energy decay rate going to zero. This occurs when the initial condition has flow structures with variation only in the z direction (Fourier modes with $k_x = k_y = 0$), because the energy in such modes grows proportionally to $\bar{L}^{-2}$ as $\bar{L} \to 0$ in the linear solution [11]. Then the fraction of energy in these modes grows during compression in the linear solution, eventually dominating the energy. At present, for the nonlinear simulations, we find that the fraction of energy in these modes decreases as the compressions progress. Thus, the smaller, and decreasing, decay power and the associated larger n_{2D} observed here appear to be "real" effects of the nonlinear system.

We now discuss a few other features observed in Figs. 2 and 3 before discussing the results of simulations utilizing a different initial condition which help to further demonstrate the key features just discussed.

The last value of $\alpha_\parallel$ for the $\bar{S}_0 \approx 10$ case in Fig. 3 is $\alpha_\parallel \sim 0.74$. As an illustration, we use this value to compute $n_{2D} \sim 2 - \alpha_\parallel/2$ from Eq. (33), which gives $n_{2D} \approx 1.63$. This is plotted as a dash-dotted line in Fig. 2(c), where it can be seen to be slightly lower than the (true) value of n_{2D}. This slight discrepancy is because χ [Eq. (34)] is nonzero, if small, as reflected in the slight slope of the $\bar{S}_0 \approx 10$ curve of $\alpha_\parallel$ at late times in Fig. 3.

At early times ($t_* \lesssim 1$) in Fig. 3, faster compressions show higher decay rates. Equation (14) for $\hat{V}_z$ has a linear damping term that is proportional to the compression rate, but also decreases with $\bar{L}$. We hypothesize that the faster initial decay rate of the parallel energy in the scaled equations is caused by stronger early-time damping of $\hat{V}_z$ at higher compression rates, combined with nonlinear transfer of parallel energy to this damped component. Since these increased rates are only present for a short time, their net effect on the energy is small, as can be observed in Fig. 3(a).

We return now to the behavior of r_E in Fig. 2. In the case of slow compression, $r_E \sim 2/3$ for a substantial amount of time $t_* \lesssim 5$, $\bar{L} \lesssim 0.8$, consistent with an initial decay that is similar to the 3D case (Fig. 3). At late times (small $\bar{L}$) the three cases have r_E growing towards 1; it natural to wonder in this regime about the relative contributions to n_{2D} of transfer to z versus direct viscous dissipation through V_x and V_y. We make this comparison by writing Eq. (22) as

$$n_{2D} = 2 - \frac{\tau_c \epsilon_{\mu,\parallel}}{E_\parallel}\left(1 + \frac{-T_\parallel}{\epsilon_{\mu,\parallel}}\right). \tag{35}$$

Then the relative contribution of transfer to E_z compared to dissipation by viscosity is given by comparing $-T_\parallel/\epsilon_{\mu,\parallel}$ to 1. This quantity is plotted versus $\bar{L}$ in Fig. 4. We can see that, in the case of $\bar{S}_0 \approx 10$, it hovers around 0.1 during the period when $r_E \approx 0.98$.

Figure 5 shows the behavior of the laboratory frame TKE components as a function of compression for the three compression rates. Evident here is that, for the initially fast compression $\bar{S}_0 \approx 10$, this small comparative transfer of energy from the growing $E_\parallel$ is sufficient to support growing E_z.

For the case $\bar{S}_0 = 10$, we plot in Fig. 6 contours of the energy spectrum for the parallel energy $E_\parallel = (V_x^2 + V_y^2)/2$ after

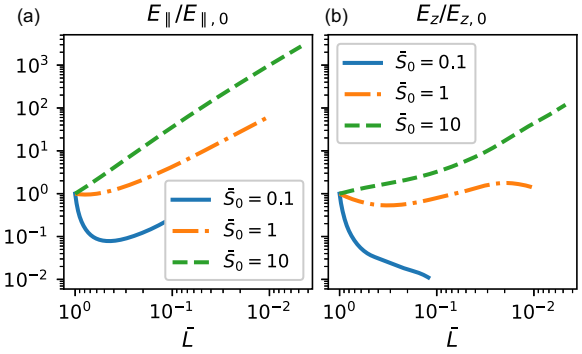

FIG. 5. Laboratory frame (unscaled) turbulent energy components (a) $E_\parallel$ and (b) E_z versus compression for the 2D compression cases shown in Fig. 2. The strong growth seen in $E_\parallel$ for the fastest initial compression rate $\bar{S}_0 \approx 10$ is associated with sustained polytropic index above the isotropic maximum $n_{2D} > 5/3$. Nonlinear transfer of energy to E_z, while a small component (see Fig. 4), is sufficient at times to cause growing or sustained E_z despite there being no direct forcing of z momentum (see Sec. III B 2 and also Sec. II).

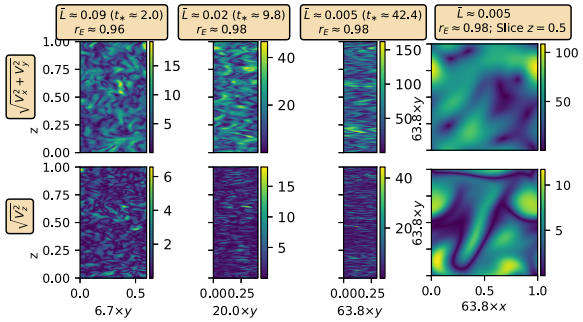

FIG. 7. Slices of the flow field during an initially rapid ($\bar{S}_0 \approx 10$) 2D compression. The top row shows the flow velocity components in the directions parallel to compression (x and y), while the bottom row shows $|v_z|$, the flow in the noncompressed z direction. The first three columns show vertical (y and z) slices through the midplane (constant x) after three different amounts of compression (increasing from left to right, with the value of $\bar{L}$ indicated in the label); the horizontal (y) direction is stretched in each plot to increase visibility. The rightmost column shows a slice at constant z for the most compressed $\bar{L}$. (See Sec. III B 2.)

summing over the y direction, $E_\parallel(k_x, k_z)$. In Fig. 6(a) the contours of $E_\parallel(k_x, k_z)$ reflect the isotropy of the initial condition. Figure 6(b) shows contours of $E_\parallel(k_x, k_z)$ after compression to $\bar{L} \approx 0.03$. By comparing Figs. 6(a) and 6(b), it can be observed that energy has primarily been added to modes with smaller k_x but across many values of k_z, with this fact causing a substantial stretching of the contours along the horizontal axis. This difference between the k_x and k_z spectral directions likely stems from the fact that dissipation at a given scale (in the moving frame) is smaller along z, as indicated by the form

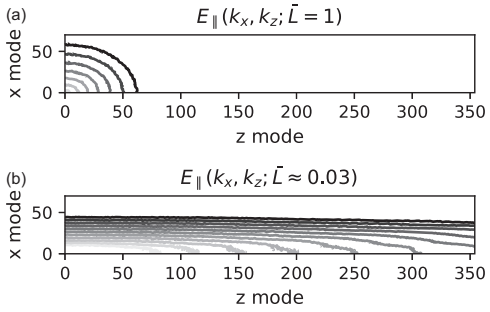

FIG. 6. For $\bar{S}_0 = 10$, contour plots of (a) the initial spectrum and (b) a compressed ($\bar{L} \approx 0.03$) spectrum for the energy in the parallel direction $E_\parallel = (V_x^2 + V_y^2)/2$ in two dimensions, showing the development of an asymmetric energy spectrum. Each contour line represents a factor of 10 change, with lighter contours representing larger values, so that the spectral energy $E_\parallel(k_x, k_z)$ generally decreases as one moves away from the origin (lower left corner) of each plot. The absolute scale is arbitrary and hence not plotted, but the plots may be compared; the largest value (lightest contour, lower left) is the same in each. In (a) this contour for the largest plotted value is essentially at (0,0). The energy spectrum $E_z(k_x, k_z)$ has very similar structure. Note that for readability we only show the quadrant with positive k_x and k_z and a subset of the z modes used the simulation.

of Eq. (10). The change in mode structure with compression is very similar for $E_z(k_x, k_z)$, although the changes in magnitude are much less dramatic, as would be indicated by the overall energy changes in Fig. 5 for $\bar{S}_0 = 10$ at $\bar{L} \approx 0.03$.

Figure 7 shows slices (vertical plane y-z) of the flow field at three points during the compression; at the last data point, it also shows slices in the x-y midplane. Here the accumulation of energy in k_z modes is observed in the fine vertical structure of the flow fields after compression. It can also be seen here that while $E_\parallel$ (V_x, V_y) dominates the energy after compression, the velocity in the noncompressed direction (z) grows as substantially as well. Because of the large amount of compression, the slices are stretched for visibility. For comparison, we also show, in Fig. 8, flow-field slices for the $\bar{S}_0 \approx 0.1$, where we can keep the actual aspect ratio.

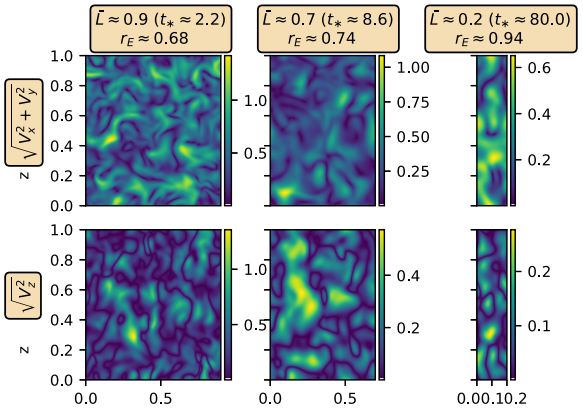

FIG. 8. Same as in Fig. 7 but for the slow compression case $\bar{S}_0 \approx 0.1$. Here the flow slices are plotted with the true aspect ratio.

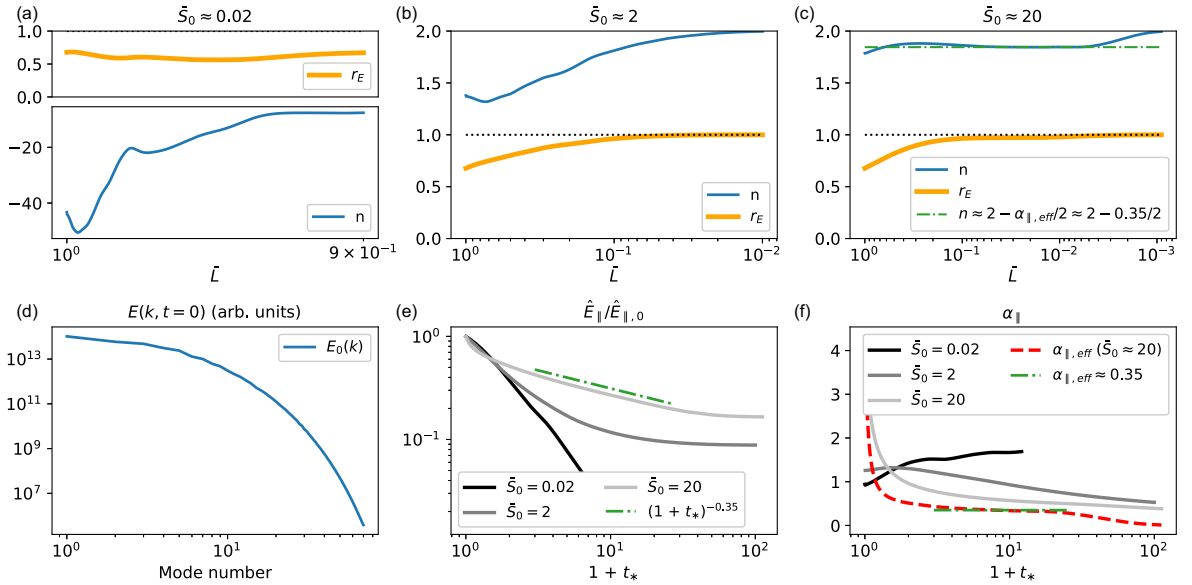

FIG. 9. Quantities of interest for 2D compression at various initial rates, as in Figs. 2 and 3 (see also 3D compression in Fig. 1). Here a different scheme is used to generate the initial state (see Sec. II), resulting in an initial-state energy spectrum with energy more concentrated in long-wavelength modes; compare (d) to Fig. 1(a), with the latter used in the prior 3D and 2D compression results. (For discussion see Sec. III C.)

C. Additional simulations for n_{2D}

Here we present results for 2D compression at varying rates, as above in Sec. III B 2, but for an initial flow state that has a different energy spectrum, shown in Fig. 9(d). The key features observed previously are again observed in Figs. 9(e) and 9(f). Namely, the scaled energy decays more slowly as a function of t_* with increasing initial compression rate $\bar{S}_0$ and the associated instantaneous inferred decay rate $\alpha_\parallel$ decreases in time (as the compression progresses).

In the case of a very slow initial compression rate $\bar{S}_0 \approx 0.02$, we see the opposite trend of an increasing decay rate in time up to the end of the simulated compression [Fig. 9(f)], consistent with the 3D case shown in Fig. 1. For this 2D compression case ($\bar{S}_0 \approx 0.02$) we may expect this trend to eventually reverse, as the aspect ratio of the domain becomes large and the x-y plane flow becomes simple (see the discussion below), although the (laboratory frame) TKE will have decayed very substantially from its initial value by this time.

The 2D compression results for n_{2D} and r_E are shown in Figs. 9(a)–9(c). The slow compression case $\bar{S}_0 \approx 0.02$ has r_E fluctuating around the isotropic value of $2/3$, while the $\bar{S}_0 \approx 2$ and 20 cases show growing r_E, with both cases eventually reaching $r_E \approx 1$ and $n_{2D} \approx 2$.

The $\bar{S}_0 \approx 20$ case shows an intermediate plateau regime in n, and in r_E. Since $\bar{L}$ is small during this regime, we can ignore the contribution of $\bar{L}(\bar{S}_0/2 - 1)$ in the denominator of n_{2D} as written in Eq. (33). We define an effective $\alpha_\parallel$,

$$\alpha_{\parallel,\mathrm{eff}} = \alpha_\parallel(1 + \chi), \tag{36}$$

so that

$$n_{2D} \sim 2 - \frac{\alpha_{\parallel,\mathrm{eff}}}{2}. \tag{37}$$

In other words, $\alpha_{\parallel,\mathrm{eff}}$ is the apparent power of the assumed decay (32) when $\alpha_\parallel$ changes in time ($\bar{L}$).

In Fig. 9(f) we show both $\alpha_\parallel$ (green solid line) and $\alpha_{\parallel,\mathrm{eff}}$ (red dashed line) for $\bar{S}_0 = 20$. Since $\alpha_\parallel$ decreases in time, χ [Eq. (34)] is negative and $\alpha_{\parallel,\mathrm{eff}} < \alpha_\parallel$ [Eq. (36)].

There is an approximate plateau at $\alpha_{\parallel,\mathrm{eff}} \approx 0.35$ (purple dash-dotted line), which matches the apparent slope of $\hat{E}_\parallel$ in Fig. 9(e). This figure also shows [Fig. 9(c)] that n_{2D} calculated using this value of $\alpha_{\parallel,\mathrm{eff}}$, through Eq. (37), matches n_{2D} during the plateau regime, $n_{2D} \approx 1.83$.

Flow slices for the $\bar{S}_0 \approx 20$ case are shown in Fig. 10, including, in the second column, slices during this plateau

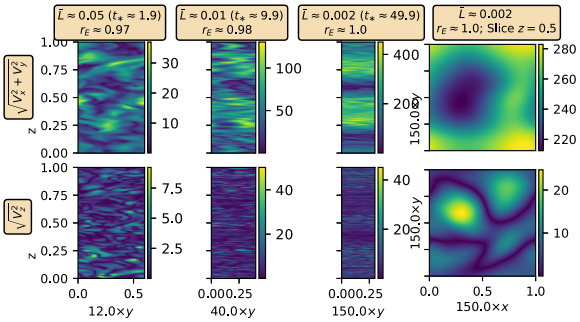

FIG. 10. Slices of the domain showing the flow field in a 2D compression at an initially fast rate ($\bar{S}_0 \approx 20$), as in Fig. 7, but with the alternate initial condition used in Fig. 9. Of note is the simple flow structure of the parallel (to compression) flow components, observed in a slice of the compression plane x-y, the top right panel. (See Sec. III C.)

regime (at $\bar{L} \approx 0.01$). During this time $r_E \approx 0.98$, and we find $-T_\parallel/\epsilon_{\mu,\parallel} \sim 0.3$, indicating that transfer of energy to the z direction still plays a role during this stage [Eq. (35)] before falling off as $n_{2D} \sim 2$.

The x-y flow slices in Fig. 10 (right column) show that, at the last simulated point ($\bar{L} \approx 0.002$ and $t_* \approx 50$), the V_x and V_y flow consists primarily of flow with a single oscillation in the domain ($k_x \sim k_y \sim 2\pi$). Compare this with the x-y flow slices (right column) in Fig. 7, for the previously discussed initial condition, which are shown after a similar magnitude of initial decay times $t_* \approx 42$; this initial condition shows a higher-mode (k_x and k_y) structure still at this time. Thus, the precompression initial state used in this section, for the results in Figs. 9 and 10, reaches a long-wavelength-dominated state more quickly, owing to its initial spectrum, and this state is seen to be associated with $n_{2D} \sim 2$.

Although a detailed analysis is beyond the scope of the present work, we now discuss, qualitatively, a possible explanation for the observed smaller (compared to 3D) decay rates of the scaled energy and for the fact that these rates decrease during the compression. It is these key features that are associated with larger n_{2D}, which can apparently be sustained even during compression at initially modest rates $\bar{S}_0 \sim 1, 2$, unlike in the 3D compression case.

As $\bar{L}$ becomes smaller, there is a tendency for the V_x and V_y Eq. (5) and (6) to have reduced relative influence from V_z and Z derivatives, as evidenced by the $\bar{L}$ scaling factors in the equations (including the continuity equation as well). If we took this to the extreme, we would drop the Z derivative term (last term) from the convective term (9), the dissipation term (10), and the continuity Eq. (8). After rescaling V_x and V_y to $\hat{V}_x$ and $\hat{V}_y$, as before, we would then have a system that, for $\beta = 3/2$, is the (unforced) 2D NS equations (we can write an equation for the scaled z vorticity to eliminate the pressure).

In true 2D turbulence, the energy decay can become negligible at high Reynolds numbers [41,42]. At present, if the energy decay in the scaled variables becomes negligible, we would find $n_{2D} \to 2$. Thus, if the effects of 2D contraction lead to a tendency toward decoupling from the V_z flow, we may expect a reduced decay of the scaled energy compared to the 3D case and an associated large and sustained growth rate for the (unscaled) energy. Since in general V_z is not decoupled from the dynamics, the 2D compression system is perhaps more akin to other 3D systems exhibiting partially reduced dimensionality [42,43].

IV. SUMMARY

Here we have studied the 2D compression of initially isotropic 3D turbulence and made a comparison to the (isotropic) 3D compression of such turbulence. In analogy with thermal energy, we may define a turbulent pressure associated with the incremental work done on (or by) the turbulence in an incremental change of volume. Then we can write a polytropic relation for this pressure $pV^n = C$ and find the polytropic (or adiabatic) index n associated with the turbulent pressure in compressions.

In the case of 3D (isotropic) compressions, n_{3D} for the turbulent pressure is $n_{3D} \leqslant 5/3$; then, in a compression that is adiabatic for the thermal energy, we will find that the rate of growth ($n_{\rm th}$) of the thermal energy is at least as large as the turbulent growth. Since, in a self-consistent adiabatic model, dissipated turbulent energy will appear as thermal energy, we expect that in general for 3D compressions $n_{\rm thermal} > n_{3D}$.

On the other hand, in a 2D compression, the compression only does work against flows in the compressed direction; if energy input into these flows is not efficiently equilibrated into the uncompressed third direction, the polytropic index for the turbulence n_{2D} may exceed the isotropic, adiabatic, value of $5/3$, $n_{2D} > 5/3$. As a result, energy input by the compression may preferentially flow into the turbulence even in a compression with adiabatic temperature growth. We find that $n_{2D} > 5/3$ can occur in 2D compressions. This is a result of sustained anisotropy of the turbulence, which we find here becomes highly anisotropic in energy content, with the vast majority of energy parallel to the plane of compression.

Moreover, we find that, compared to 3D compression at a similar rate, turbulence in 2D compressions can be more easily sustained or enhanced; this is reflected by the behavior of the scaled energy at late times. In three dimensions, this scaled energy experiences an increasing decay rate at late times (large compression), associated with late stage decay of turbulence. In two dimensions, the comparable scaled energy experiences a decreasing decay rate at late times (large compression); this decrease is likely due to the large aspect ratio of such 2D compressions at late times, which causes a tendency toward two-dimensionalization.

When $n_{2D} > 5/3$, the turbulent Mach number may increase with compression as the turbulence is preferentially enhanced relative to the thermal energy. We can make a simple estimate of an extreme (adiabatic) case by taking $n_{2D} = 2$ and $n_{\rm th} = 5/3$. Then the Mach number (normalized to initial value $\bar{M}$) for the parallel flow will scale as $\bar{M} \sim \bar{V}^{(n_{\rm th}-n_{2D})/2} \sim \bar{V}^{-1/6}$; a doubling would require a compression in volume ($\bar{V} = V/V_0$) by a factor of approximately 64. This simple estimate ignores the flow of dissipated turbulence into thermal energy, which would tend to increase $n_{\rm thermal}$, but which diminishes as $n_{2D} \to 2$. It also assumes adiabatic increase of the thermal energy; in general, conduction, radiation, or other loss mechanisms will reduce the polytropic (adiabatic) index of the thermal energy in the compression, enhancing the effect.

Throughout, we have used periodic boundary conditions. One result of this is that $k_x = k_y = 0$ Fourier modes, which can be linearly important in the 2D compression problem [11], are permitted; however, we find that the energy in such modes generally decreases in the present simulations. More generally, physical boundary conditions, say, associated with a cylindrical liner in MagLIF experiments, should be considered; such boundary conditions may provide damping at large scales, which could, for instance, reduce the observed values of n_{2D}. The present treatment neglects any electric or magnetic fields; some existing laboratory experiments which compress plasma in two dimensions have (strong) applied magnetic fields, the effects of which may then be important in turbulence dynamics. Nevertheless, if they do not tend to help maintain isotropy, some of the intuition from the present work may still hold.

The compressions considered here proceed with a constant (compression) velocity $L \propto U_b t$ [Eq. (2)]. This preserves spatial homogeneity in the equations when the background

pressure is assumed to be uniform in space [5,24,30], greatly simplifying the present analysis of the turbulence. In various compression experiments, including Z-pinch compressions such as MagLIF, the compression velocity changes in time. This case can be treated in the present framework by considering a background pressure which depends on space [5,24,30], but then for consistency with the ideal gas law, the temperature (and therefore viscosity) would depend on space, breaking homogeneity. Nevertheless, to the extent the turbulence results do not depend on the changing viscosity (due to high Reynolds number), the present framework could treat this case.

More generally, if we allow for density perturbations, a term associated with the accelerating compression enters the momentum equation [30]. We now roughly estimate the size of this term compared with the compression forcing term due to volumetric contraction considered here [e.g., the second term on the left-hand side of Eq. (4) and similarly for two dimensions], for a specific case. The ratio of this acceleration term to the volumetric forcing is of the magnitude $[\rho'/(\bar{\rho}+\rho')](\ddot{L}x/\dot{L}v')$. Here ρ' is the density perturbation and $\bar{\rho}$ the mean density. We assume that the flows are relatively compressible so that $\rho' \sim \bar{\rho}$ and this term is order unity, leaving us with the ratio $\ddot{L}x/\dot{L}v'$.

As an example, we estimate this ratio in the case of an analytic liner solution used in [14], where the liner radius $r = r_0(1-\tau^4)$, with r_0 the initial radius and τ a normalized time, $\tau \in [0, 1]$. While the acceleration term varies spatially (for example, vanishing at $x = 0$), we take $x \sim r$. Then we take the perturbed velocity $v' \propto \dot{r}$ [in a special case of 3D compression, it can be shown that v' nonlinearly saturates slightly above the compression velocity (see Ref. [5]); in the present 2D case, the tendency toward two-dimensionalization may relax this saturation cap]. With these assumptions we will find $\ddot{L}x/\dot{L}v' \sim (1-\tau^4)/\tau^4$.

In this estimation, for this particular analytic liner solution, the acceleration term is more important for $r \gtrsim r_0/2$, while the volumetric forcing considered here is more important for $r \lesssim r_0/2$. If density perturbations are small compared to the mean density, then the relative magnitude of this acceleration term will be reduced and the compression term will be dominant for a larger fraction of the compression. In any event, we note that the 2D compression momentum equations considered here [Eqs. (5)–(7)] depend explicitly on $\bar{L}(t)$ and so even if the acceleration term can be dropped, the time history of the compression will matter in general.

While we have highlighted potential relevance to various Z-pinch compression experiments, the present work may find relevance elsewhere as well, for example, possibly in astrophysical situations that produce (quasi-)2D contractions in elongated structures (such as shock-compressed gas pillars in molecular clouds or jets) or perhaps in contractions in gas dynamics, though the Z-pinch contractions tend to cause much larger total volume contraction than many other applications.

Overall, we hope the present work helps to call attention to essential differences in the behavior of bulk turbulence under compression when compressed in two versus three dimensions and the possibility for anisotropy to lead to enhance turbulent growth in two dimensions when compared to three.

ACKNOWLEDGMENTS

This work was performed under the auspices of the US Department of Energy by the Lawrence Livermore National Laboratory under Contract No. DE-AC52-07NA27344. This document was prepared as an account of work sponsored by an agency of the United States government. Neither the US government nor Lawrence Livermore National Security, LLC, nor any of their employees makes any warranty, expressed or implied, or assumes any legal liability or responsibility for the accuracy, completeness, or usefulness of any information, apparatus, product, or process disclosed, or represents that its use would not infringe privately owned rights. Reference herein to any specific commercial product, process, or service by trade name, trademark, manufacturer, or otherwise does not necessarily constitute or imply its endorsement, recommendation, or favoring by the US government or Lawrence Livermore National Security, LLC. The views and opinions of authors expressed herein do not necessarily state or reflect those of the US government or Lawrence Livermore National Security, LLC, and shall not be used for advertising or product endorsement purposes.

S.D. would also like to acknowledge the support of the US Department of Energy Fusion Energy Sciences Postdoctoral Research Program administered by the Oak Ridge Institute for Science and Education (ORISE) for the DOE. ORISE is managed by Oak Ridge Associated Universities under DOE Contract No. DE-SC0014664. This work was supported, in part, by NSF Grant No. PHY-1805316 and NNSA Grant No. 83228-10966 [Prime No. DOE (NNSA) DE-NA0003764].

[1] B. Robertson and P. Goldreich, Astrophys. J. Lett. **750**, L31 (2012).
[2] S. Davidovits and N. J. Fisch, Astrophys. J. **838**, 118 (2017).
[3] Y. Birnboim, C. Federrath, and M. Krumholz, Mon. Not. R. Astron. Soc. **473**, 2144 (2017).
[4] S. Davidovits and N. J. Fisch, Phys. Rev. Lett. **116**, 105004 (2016).
[5] S. Davidovits and N. J. Fisch, Phys. Rev. E **94**, 053206 (2016).
[6] S. Davidovits and N. J. Fisch, Phys. Plasmas **24**, 122311 (2017).
[7] G. Viciconte, B.-J. Gréa, and F. S. Godeferd, Phys. Rev. E **97**, 023201 (2018).
[8] A. Campos and B. E. Morgan, Phys. Rev. E **99**, 013107 (2019).
[9] A. Campos and B. E. Morgan, Phys. Rev. E **99**, 063103 (2019).
[10] S. Davidovits and N. J. Fisch, Phys. Plasmas **26**, 062709 (2019).
[11] S. Davidovits and N. J. Fisch, Phys. Plasmas **26**, 082702 (2019).
[12] E. Kroupp, E. Stambulchik, A. Starobinets, D. Osin, V. I. Fisher, D. Alumot, Y. Maron, S. Davidovits, N. J. Fisch, and A. Fruchtman, Phys. Rev. E **97**, 013202 (2018).
[13] D. D. Ryutov, M. S. Derzon, and M. K. Matzen, Rev. Mod. Phys. **72**, 167 (2000).

[14] S. A. Slutz, M. C. Herrmann, R. A. Vesey, A. B. Sefkow, D. B. Sinars, D. C. Rovang, K. J. Peterson, and M. E. Cuneo, Phys. Plasmas **17**, 056303 (2010).
[15] S. A. Slutz and R. A. Vesey, Phys. Rev. Lett. **108**, 025003 (2012).
[16] E. Kroupp, D. Osin, A. Starobinets, V. Fisher, V. Bernshtam, L. Weingarten, Y. Maron, I. Uschmann, E. Förster, A. Fisher, M. E. Cuneo, C. Deeney, and J. L. Giuliani, Phys. Rev. Lett. **107**, 105001 (2011).
[17] Y. Maron, A. Starobinets, V. I. Fisher, E. Kroupp, D. Osin, A. Fisher, C. Deeney, C. A. Coverdale, P. D. Lepell, E. P. Yu, C. Jennings, M. E. Cuneo, M. C. Herrmann, J. L. Porter, T. A. Mehlhorn, and J. P. Apruzese, Phys. Rev. Lett. **111**, 035001 (2013).
[18] D. Alumot, E. Kroupp, E. Stambulchik, A. Starobinets, I. Uschmann, and Y. Maron, Phys. Rev. Lett. **122**, 095001 (2019).
[19] B. Jones, C. Deeney, C. Coverdale, P. LePell, J. McKenney, J. Apruzese, J. Thornhill, K. Whitney, R. Clark, A. Velikovich, J. Davis, Y. Maron, V. Kantsyrev, A. Safronova, and V. Oreshkin, J. Quant. Spectrosc. Radiat. Transfer **99**, 341 (2006).
[20] B. Jones, J. P. Apruzese, A. J. Harvey-Thompson, D. J. Ampleford, C. A. Jennings, S. B. Hansen, N. W. Moore, D. C. Lamppa, D. Johnson, M. C. Jones *et al.*, Phys. Plasmas **22**, 020706 (2015).
[21] E. Yu, F. Doss, and M. Weis, Vortex generation, amplification, and mix in MagLIF: A work in progress, Technical Report No. SAND2019-9390C, Sandia National Laboratories, 2019 (unpublished).
[22] C.-T. Wu, J. H. Ferziger, and D. R. Chapman, Stanford University, Technical Report No. TF-21, Department of Mechanical Engineering, 1985 (unpublished).
[23] C. Cambon, G. N. Coleman, and N. N. Mansour, J. Fluid Mech. **257**, 641 (1993).
[24] G. A. Blaisdell, Numerical simulation of compressible homogeneous turbulence, Ph.D. thesis, Stanford University, 1991.
[25] G. Coleman and N. Mansour, in *Turbulent Shear Flows 8*, edited by F. Durst, R. Friedrich, B. Launder, F. Schmidt, U. Schumann, and J. Whitelaw (Springer, Berlin, 1993), pp. 269–282.
[26] S. I. Braginskii, Rev. Plasma Phys. **1**, 205 (1965).
[27] S. Davidovits and N. J. Fisch, Phys. Plasmas **25**, 042703 (2018).
[28] C. R. Weber, D. S. Clark, A. W. Cook, L. E. Busby, and H. F. Robey, Phys. Rev. E **89**, 053106 (2014).
[29] T. Ishihara, T. Gotoh, and Y. Kaneda, Annu. Rev. Fluid Mech. **41**, 165 (2009).
[30] C. Cambon, Y. Mao, and D. Jeandel, Eur. J. Mech. B **11**, 683 (1992).
[31] K. J. Burns, G. M. Vasil, J. S. Oishi, D. Lecoanet, and B. P. Brown, Phys. Rev. Res. **2**, 023068 (2020).
[32] T. S. Lundgren, *Annual Research Briefs* (Center for Turbulence Research, Stanford, 2003), pp. 461–473.
[33] C. Rosales and C. Meneveau, Phys. Fluids **17**, 095106 (2005).
[34] P. Sagaut and C. Cambon, *Homogeneous Turbulence Dynamics* (Cambridge University Press, New York, 2008).
[35] M. Sinhuber, E. Bodenschatz, and G. P. Bewley, Phys. Rev. Lett. **114**, 034501 (2015).
[36] M.-M. Mac Low, Astrophys. J. **524**, 169 (1999).
[37] P. G. Saffman, Phys. Fluids **10**, 1349 (1967).
[38] L. Skrbek and S. R. Stalp, Phys. Fluids **12**, 1997 (2000).
[39] B. Thornber, Phys. Fluids **28**, 045106 (2016).
[40] D. Lohse, Phys. Rev. Lett. **73**, 3223 (1994).
[41] A. Bracco, J. C. McWilliams, G. Murante, A. Provenzale, and J. B. Weiss, Phys. Fluids **12**, 2931 (2000).
[42] G. Boffetta and R. E. Ecke, Annu. Rev. Fluid Mech. **44**, 427 (2012).
[43] A. Celani, S. Musacchio, and D. Vincenzi, Phys. Rev. Lett. **104**, 184506 (2010).